Catalysis Science & Technology

Accepted Manuscript

This article can be cited before page numbers have been issued, to do this please use: A. K. Kar, S. P. Kaur, D. T. J. Kumar and R. Srivastava, *Catal. Sci. Technol.*, 2020, DOI: 10.1039/D0CY01279C.

ROYAL SOCIETY OF CHEMISTRY

rsc.li/catalysis

View Article Online
DOI: 10.1039/D0CY01279C

Efficient hydrogenolysis of aryl ethers over Ce-MOF supported Pd NPs under mild conditions: Mechanistic insight using density functional theoretical calculations

Ashish Kumar Kar[a], Surinder Pal Kaur[a], T. J. Dhilip Kumar[a] and Rajendra Srivastava[a]*

[a]*Catalysis Research Laboratory, Department of Chemistry, Indian Institute of Technology Ropar, Rupnagar, Punjab-140001, India*

*Email: rajendra@iitrpr.ac.in

**Phone: +91-1881-242175; Fax: +91-1881-223395*

View Article Online
DOI: 10.1039/D0CY01279C

Abstract

Selective hydrogenolysis of lignin-derived aryl ethers under mild temperature and pressure is an important milestone to be achieved to fulfill the future fuel demands from abundantly available biomass resources. Selective hydrogenolysis requires precise modulation of surface active sites of the catalyst to obtain the desired activity and selectivity. In this study, the selective hydrogenolysis of benzyl phenyl ether to phenol and toluene is achieved in methanol and water medium at a very low temperature and low H_2 pressure over Pd nanoparticles decorated Ce-BTC metal-organic framework. The activity of the developed catalyst is two times higher than that of Pd decorated CeO_2. Structure-activity relation is established using catalytic measurements, X-ray photoelectron spectroscopy, and transmission electron microscopy. The mechanistic insight into the hydrogenolysis of aryl ethers and the reasons behind the superior activity of Pd/Ce-BTC than Pd/CeO_2 are investigated using the density functional theoretical (DFT) calculations. Spectroscopic measurements and DFT calculations suggest that the higher Pd^0/Pd^{2+} ratio and higher adsorption of benzyl phenyl ether over Pd/Ce-BTC and higher adsorption of phenol over Pd/CeO_2 are factors responsible for the higher activity of Pd/Ce-BTC than Pd/CeO_2. Efficient recyclability and hot filtration test reveal that the catalyst exhibits no noteworthy loss in the activity after five consecutive cycles. The Pd/Ce-BTC displays very high turnover frequency and low activation energy, which are very attractive from the industrial perspective and academic points of view.

View Article Online
DOI: 10.1039/D0CY01279C

Introduction

Biomass can replace fossil fuels and can acts as a feedstock for liquid fuels and chemicals in the coming years.[1,2] It is estimated that only less than 10% of biomass is utilized, and the rest is just discarded or burnt. Biomass contains lignin, cellulose, and hemicelluloses.[3-5] Significant research is being carried out to convert cellulose and hemicelluloses to furfural and 5-hydroxymethyl furfural as platform chemicals to produce a broad range of furan based chemicals.[6-9] State of the art catalytic conversion of furfural and 5-hydroxymethyl furfural, especially by oxidative and reductive up-gradation protocols, using conventional catalytic, photocatalytic, and electrocatalytic strategies is recently documented.[10] The selective reduction/oxidation of furan based feedstocks can fulfill the fuel and polymer industries demand.[11,12] Lignin, a polymeric network structure is composed of phenolic and aromatic building blocks that are bonded with each other via C-C and C-O bonds.[13-15] The selective depolymerization of lignin can meet the demands for aromatic liquid fuels and fine chemicals without depending upon fossil fuel resources.[16-19] This can be achieved only when the benzene ring is unaffected during the lignin depolymerization process. Gasification, liquefaction, and pyrolysis are the most common techniques that have been adopted for the depolymerization of lignin.[20-23] However, the poor control over product selectivity due to harsh reaction condition makes these techniques unfavorable and non-facile for lignin depolymerization. Hydrogenolysis, a catalytic tool is being studied extensively for the lignin depolymerization.[21-23] The development of a robust redox catalyst for the hydrogenolysis of aryl ethers during the reductive catalytic fractionation of lignocellulosic biomasses, aka "lignin-first biorefinery" will play a key role in obtaining high yield of monophenols.[24-25] However, the challenge is to find a catalyst that maintains excellent product selectivity under mild reaction conditions. In addition to this, unravelling the mechanistic pathway and understanding the insights of this hydrogenolysis reaction is also a challenging task. Extreme care should be taken in developing a catalyst and process parameters for the selective hydrogenolysis because the aromatic compounds should not be hydrogenated during this process and loose its aromaticity.[26] The lignin constitutes approximately 80% ether linkages; therefore, one can select aromatic compounds having ether linkage as model reactants to demonstrate the effectiveness of the developed catalyst in hydrogenolysis.[26,27]

Many homogeneous and heterogeneous catalysts have been developed for the hydrogenolysis of aromatic ethers.[28-39] Homogenous metal (based on V, Ni, and Ru) catalysts can be operated under mild conditions (<423 K) for the selective ether cleavage.[28-30]

View Article Online
DOI: 10.1039/D0CY01279C

However, the developed homogeneous complexes are water-sensitive, and recovery & recycling of such catalysts are not feasible; therefore, the development of heterogeneous catalysts is essential. Heterogeneous catalysts based on Ni and Pd (supported on zeolites and metal oxides) are developed.[31-33] However, these catalysts are less selective for the ether bond, and cleavage & reduction of arenes also takes place during the reaction. Later, porous SiC supported Ni nanoparticles (NPs) catalyst is developed, which is found to be stable and recyclable during the selective cleavage of ether bonds for various lignin-based model compounds in the presence of KOtBu.[34] A Ni/C catalyst is reported for the selective cleavage of a lignin model compound, benzyl phenyl ether (BPE), using $NaBH_4$.[35] This catalyst provides better activity than Pd/C, Ru/C, and Rh/C. Ni-H catalyst based on a metal-organic framework (MOF) which constitutes Ti in different oxidation states (as $Ti^{III}Ti^{IV}$) is developed for the hydrogenolysis of benzyl phenyl ether at 413 K.[36] Another Ti-based catalyst; titanium nitride-Ni nanocomposite is developed for the hydrogenolysis of aryl ethers in ethanol at mild reaction conditions (12 bar H_2 pressure and 398-423 K).[37] Very recently Pd-Pt bimetallic catalyst is developed for the hydrogenolysis of lignin model compounds that can be operated under mild reaction conditions.[38] Moreover, Pd based catalyst is developed for the selective ether cleavage via transfer hydrogenolysis of benzyl phenyl ether using 2-propanol as an H-donor.[39] However, it requires a significantly higher temperature of 513 K for the selective cleavage of the ether C–O bond.

The literature reports suggest that supported small size Pd NPs catalysts are effective for the selective hydrogenolysis of aryl ethers.[40-43] The high surface energy of small-sized metal NPs facilitates the aggregation or fusion of metal NPs during the catalytic process.[44,45] However, the use of sacrificial support could stabilize the metal NPs by minimizing the aggregation or fusion process.[46] Unfortunately, this aggregation phenomenon has a negative effect on the catalytic efficiency during catalysis using existing support matrixes such as zeolites, silica, carbon, metal oxides etc.[47] Thus, the confinement of the small size metal NPs in a particular oxidation state during the catalytic operation is a challenging task. Metal-organic framework (MOF) is a nanoporous material containing metal centers or metal clusters connected with multi-dentate organic molecules as bridging ligands to get a multifunctional networking structure.[48] The inherent nature of MOF materials, including high density and spatial distribution of active sites around the framework and the presence of open porous channels, enables the easy accessibility of the active sites that facilitates the diffusion phenomena, making MOF materials a benchmark candidate in the field of catalysis.[49] The spatial arrangement of active sites and the presence of the coordinative unsaturated sites

View Article Online
DOI: 10.1039/D0CY01279C

present in the multifunctional MOF provides phenomenal stability to the embedded metal NPs.[50]

This study aims to find a MOF based catalyst with optimum bonding with aryl ethers & their hydrogenolysis products and provides a strategy to effectively encapsulate and stabilize Pd NPs to achieve excellent activity and recyclability. Herein, Pd NPs decorated Ce-BTC MOF is synthesized for the selective hydrogenolysis of aryl ethers under mild temperature and pressure. The activity of Pd NPs decorated Ce-MOF is two-fold higher than that of Pd NPs decorated CeO_2 under identical reaction conditions. To obtain the mechanistic insights and the reasons behind Pd/Ce-BTC's superior activity than Pd/CeO_2, the density functional theoretical (DFT) calculations are carried out. The catalyst exhibits excellent recyclability and better catalytic activity (turn over frequency) than various catalysts reported in the literature.

Results and discussion

Powder XRD pattern of Ce-BTC exhibits distinguished diffraction peaks suggesting the highly crystalline nature of the material. The XRD pattern of the Ce-BTC matches well with the simulated XRD pattern of La-BTC MOF (Fig. 1A).[51,52] The absence of additional peaks confirms the phase purity and monoclinic crystal structure and space group (Cc) of La-BTC MOF.[51,52] The XRD patterns of Pd supported Ce-BTC materials (Pd/Ce-BTC) are very similar to the parent Ce-BTC, suggesting that Ce-BTC was highly stable under the reducing synthesis condition. No distinguished diffractions corresponding to Pd NPs are observed in the materials implying that a low amount of Pd (0.5 wt% to 2.5 wt %) in a highly dispersed state with tiny size is embedded in Ce-BTC matrix.

Ce-BTC exhibits type II/IV isotherm with H3 hysteresis ((Fig. 1B). The material displays low adsorption in the P/P_0 of 0-0.8, followed by the steep adsorption. The steep adsorption above 0.8 (P/P_0) suggests that the adsorption occurs within the inter-particle void space present in the material. Upon Pd loading, the feature of adsorption does not change, but the adsorption volume increases. Pd loading provides the highly dispersed nanosize Pd particles over the surface that provides additional sites for N_2 adsorption. Thus the adsorption volume increases with an increase in the Pd loading, but beyond 1.5 wt% Pd loading, the surface area starts decreasing. Higher Pd loading decreases the Pd dispersion; therefore, the surface area slightly diminishes for Pd(2.5%)/Ce-BTC. The highest surface area is observed for Pd(1.5%)/Ce-BTC. The amount of Pd embedded in Ce-BTC was determined from elemental analysis (Microwave-plasma atomic emission spectroscopy). The amount of Pd

View Article Online
DOI: 10.1039/D0CY01279C

embedded in Pd(0.5%)/Ce-BTC, Pd(1.5%)/Ce-BTC, and Pd(2.5%)/Ce-BTC, are 0.46 wt%, 1.43 wt%, and 2.37 wt%, respectively, which are marginally lower than that of input Pd amount.

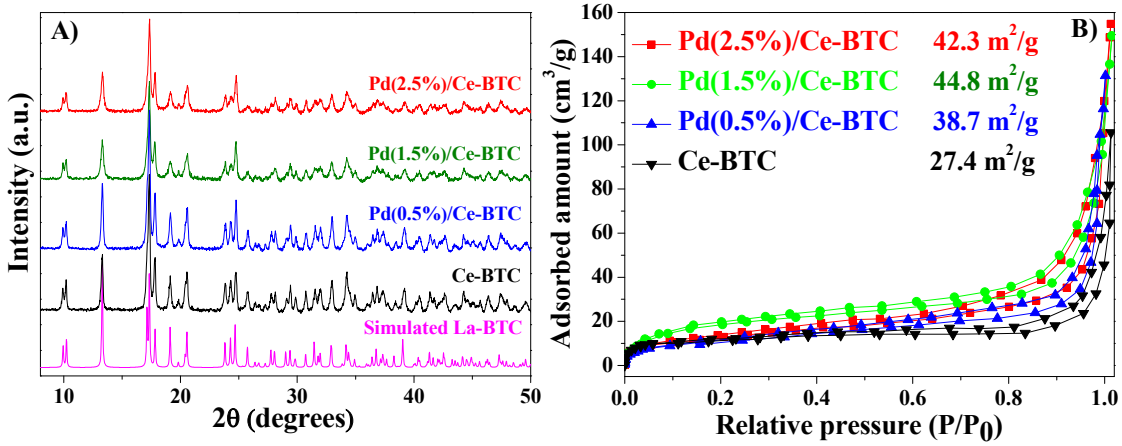

Fig. 1 (A) Powder XRD patterns of Ce-BTC and Pd/Ce-BTC materials along with simulated XRD pattern of La-BTC, and (B) N_2 adsorption-desorption isotherms of Ce-BTC and Pd/Ce-BTC materials.

The thermogravimetric analysis (TGA) shows that a weight loss in 298-423 K is due to the removal of loosely bound water (physisorbed or weakly bonded) or ethanol molecules (Fig. S1). The weight loss in the range of 623 K-673 K is due to the framework decomposition during the heat treatment process in TGA measurement. TGA experiments suggest that Ce-BTC MOF can be employed in the temperature up to 623 K (preferably less than 573 K).

The field emission-scanning electron microscope (FE-SEM) image shows the micrometer-sized rod-like morphology with nanometre rod thickness for Ce-BTC. No distinguished Pd particles are observed in the Pd(0.5%)/Ce-BTC during FE-SEM investigation suggesting the occurrence of nanometer-sized NPs in the Ce-MOF matrix (Fig. 2A). However, with an increase in the Pd loading, the surface roughness increases (Fig. 2B-D). Thus to get in-depth information about the dispersion of Pd NPs in Ce-BTC, high-resolution TEM images were recorded. Nanorod morphology is evident in the low-resolution TEM image (Fig. 2E1). The high-resolution TEM (HRTEM) image shows the adherence of ultra-small Pd NPs to the surface of Ce-MOF (Fig. 2E2-E3). The EDS spectrum obtained from HRTEM confirms the presence of Pd NPs on Ce-BTC MOF (Fig. S2). The elemental mapping of Pd(1.5%)/Ce-BTC MOF reveals the homogeneous distribution of highly

View Article Online
DOI: 10.1039/D0CY01279C

dispersed tiny Pd NPs. Various elements present in the material with different color code is presented in Fig. S2. From the HR-TEM image, lattice fringes corresponding to PdNPs are shown that demonstrate the presence of (111) planes of Pd NPs with d spacing of 0.221 nm (Fig. S3)

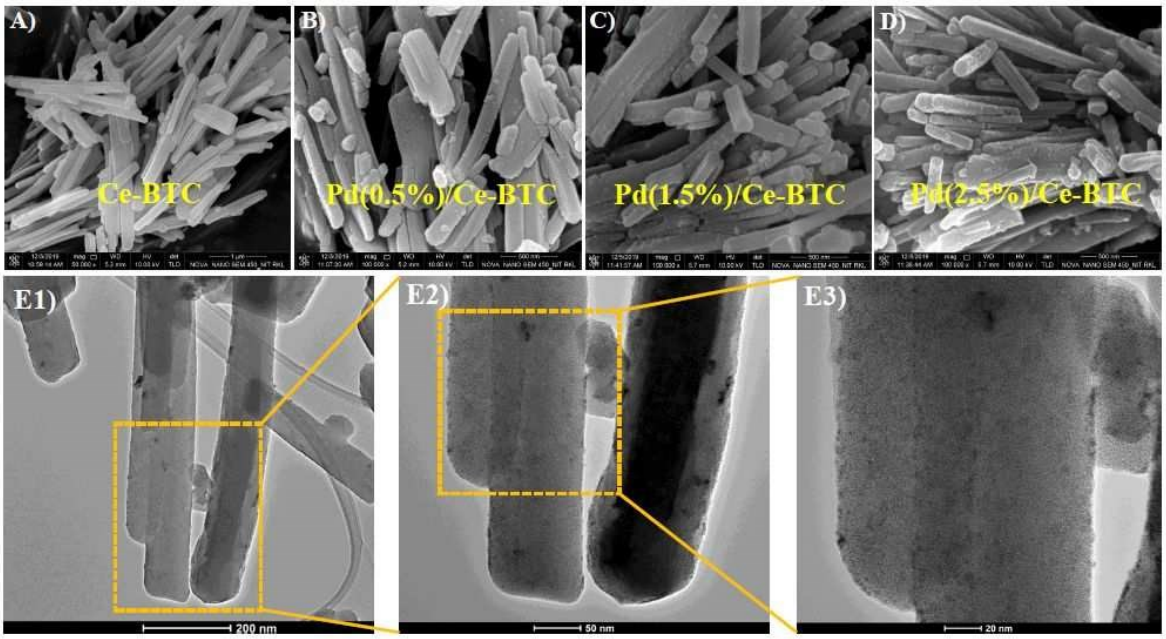

Fig. 2 FE-SEM images of (A) Ce-BTC, (B**)** Pd(0.5 %)/Ce-BTC, (C) Pd(1.5 %)/Ce-BTC, and (D) Pd(2.5 %)/Ce-BTC. (E1) TEM image and (E2-E3) HRTEM images of Pd(1.5 %)/Ce-BTC.

The surface elemental composition and oxidation states of constituent elements were determined from the X-ray photoelectron spectrometer (XPS). The surface survey profile suggests the existence of Ce, C, O, and Pd (Fig. 3 & Fig. S4). The high-resolution XPS spectra of all elements were recorded and deconvoluted (Fig. 3). XPS spectra are obtained by correcting the experimentally observed binding energies to adventitious carbon 1s standardized at 284.8 eV. The high-resolution C 1s spectrum suggests the presence of aromatic C=C/C-C corresponding to trimesic acid at 285.1 eV in addition to various C-O species (Fig. S4). The deconvoluted peaks at 285.6, 289.1, and 291 eV correspond to C-OH, C=O, and –COOH species, respectively, of the Ce-BTC framework. The high-resolution O 1s spectrum suggests the presence of a low concentration of surface adsorbed oxygen species

View Article Online
DOI: 10.1039/D0CY01279C

(534.2 eV) after the deconvolution of the O 1s signal. The deconvoluted peaks at 532.3, 531.8, and 529.8 eV correspond to C-OH, C=O, and Ce-O species, respectively, of the Ce-BTC framework (Fig. S4). The high-resolution surface Ce 3d spectrum suggests that the higher concentration of Ce is present as Ce^{4+} ($3d^{5/2}$ and $3d^{3/2}$ occur at 886.1 eV and 904.3 eV, respectively) than Ce^{3+} ($3d^{5/2}$ and $3d^{3/2}$ occur at 882.6 eV and 900.8 eV, respectively) (Fig. 3A) in Pd/Ce-BTC. The high resolution surface Pd 3d spectrum suggests that the higher concentration of Pd is present as Pd^0 ($3d^{5/2}$ and $3d^{3/2}$ occur at 335.6 eV and 340.9 eV, respectively) than Pd^{2+} ($3d^{5/2}$ and $3d^{3/2}$ occur at 337.8 eV and 342.7 eV, respectively) (Fig. 3B) in Pd/Ce-BTC. The XPS spectrum also reveals the higher ratio of Pd^0/Pd^{2+} species, which is calculated to be 2.8 for Pd(1.5%)/Ce-BTC. Similarly, the ratio of Pd^0/Pd^{2+} for Pd/CeO_2 is calculated to be 1.5. Hence, the Pd/(1.5%)/Ce-BTC would exhibit higher activity due to the presence of predominant Pd^0 species compared to Pd/CeO_2.

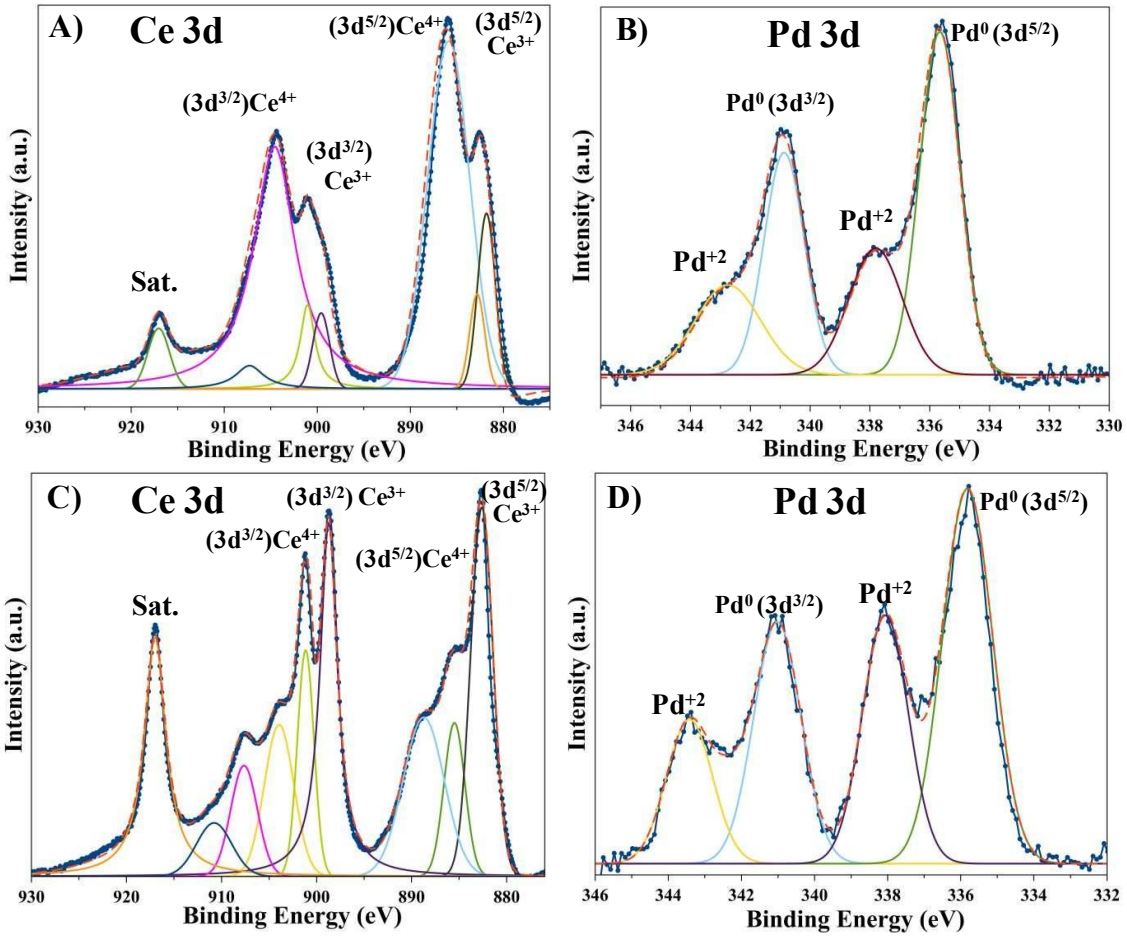

Fig. 3 The high resolution XPS spectra of (A) Ce & (B) Pd present in Pd(1.5%)/Ce-BTC and (C) Ce & (D) Pd present in $Pd(1.5\%)/CeO_2$.

View Article Online
DOI: 10.1039/D0CY01279C

The Pd/Ce-BTC catalysts are investigated in the highly important and interesting C-O hydrogenolysis reaction of lignin model compound, benzyl phenyl ether (BPE). As illustrated in the introduction section that it is essential to develop a catalyst that can be employed under very mild reaction conditions; therefore, in this study, mild reaction conditions are established. Various catalysts are compared at a reaction condition given in the footnote of Fig. 4. All the support materials Ce-BTC, CeO_2, and SBA-15 are inactive for the C-O hydrogenolysis of BPE (Fig. 4). At the same time, the Pd incorporated catalysts are found active for this reaction. Selective hydrogenolysis of BPE produces an almost equal amount of phenol and toluene (52 & 48) with no side product. The effect of Pd loading and other reaction parameters are evaluated. With an increase in the Pd loading from 0.5 wt% to 1.5 wt% in the catalyst, catalytic activity increases, and almost complete conversion is obtained using 1.5 wt% Pd (Fig. 5A). The activity of Pd(2.5%)/Ce-MOF is found to be similar. If TOF is compared, then Pd(0.5%)/Ce-BTC exhibits the best activity, but to obtain the complete conversion, Pd(1.5%)/Ce-BTC is chosen for further study. The activity of Pd(1.5%)/Ce-BTC is two times and three times higher than Pd/CeO_2 and Pd/SBA-15, respectively, suggesting that Pd incorporation in Ce-BTC is essential and highly favorable for this reaction. After finding the best catalyst, the catalyst amount is investigated from 3 mg to 12 mg (for 0.5 mmol of the BPE) (Fig. 5B). Complete conversion is achieved with 12 mg of the sample. Thus, 12 mg is chosen for further study. Catalytic investigations are carried out under optimized reaction conditions in methanol and ethanol in the absence of H_2 to rule out the possibility of the occurrence of transfer hydrogenation. Under our reaction condition using the best catalyst, no significant BPE conversion (<1 %) is observed. The influence of H_2 pressure is investigated. In contrast to previous reports, this catalyst exhibits excellent activity at a low pressure of 2 bar. The reaction also proceeds at ambient pressure in a balloon filled H_2, but at this condition, comparatively lower activity is obtained (23.1 % BPE conversion and 53% phenol and 47% toluene selectivity).

View Article Online
DOI: 10.1039/D0CY01279C

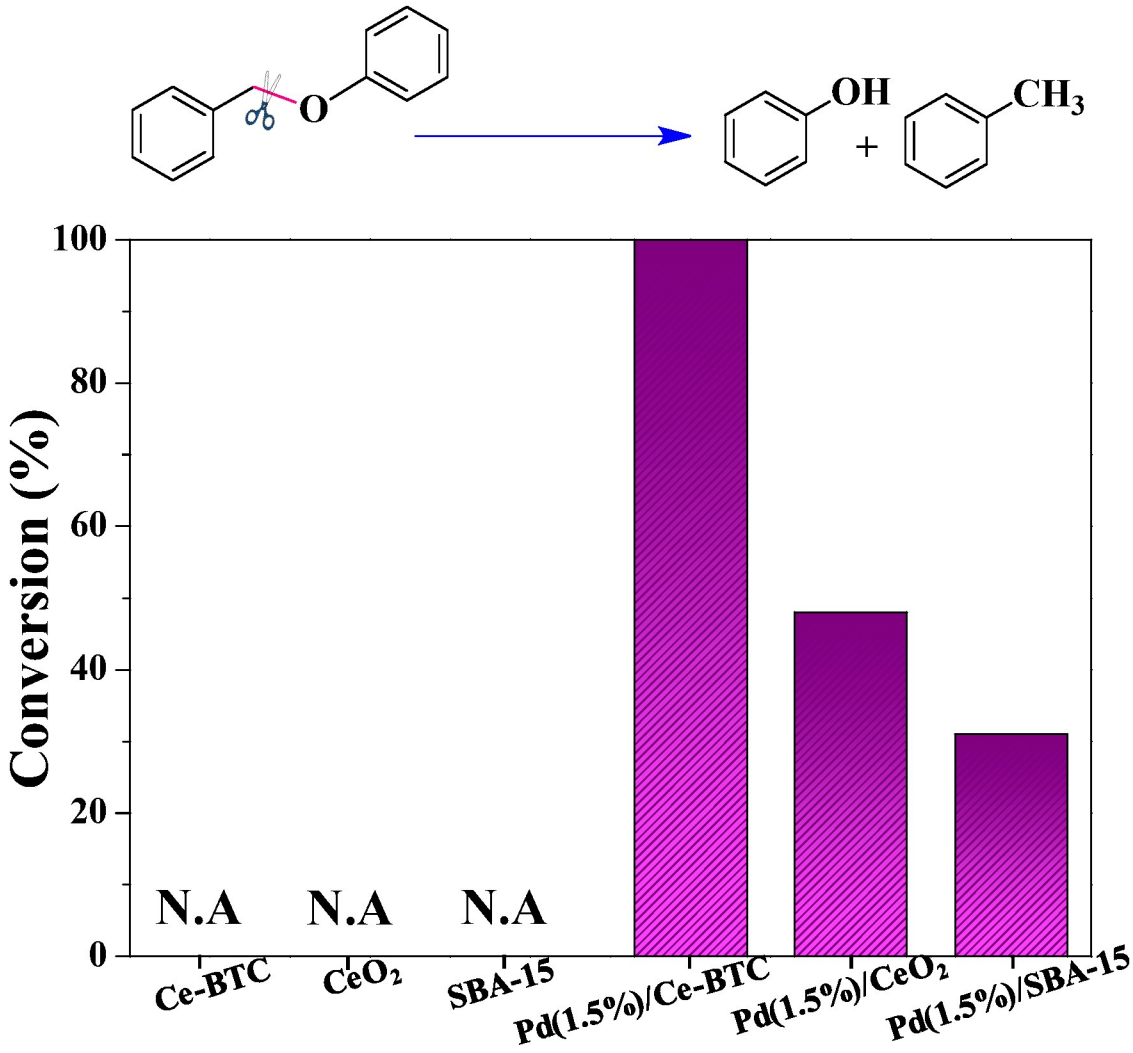

Fig. 4 C-O hydrogenolysis of BPE over various catalysts of this study. Reaction condition: BPE (0.5 mmol), catalyst (12 mg), H_2 pressure (2 bar), methanol (10 mL), temperature (353 K), time (1 h).

The reaction proceeds even at a very low temperature of 323 K, but the BPE conversion is only 21% after one hour (Fig. 5C). Reaction profiles obtained at different temperatures and at different time intervals are presented in Fig. 5C. Complete conversion is achieved by increasing the reaction temperature to 353 K. Further –ln [BPE] vs. time profile at different temperatures suggests that it follows a linear fitting that corresponds to first-order kinetics (Fig. 5D). The activation energy for BPE hydrogenolysis is calculated to be 51.62 kJ/mole over Pd(1.5%)/Ce-BTC using the Arrhenius equation (Fig. 5E).

View Article Online
DOI: 10.1039/D0CY01279C

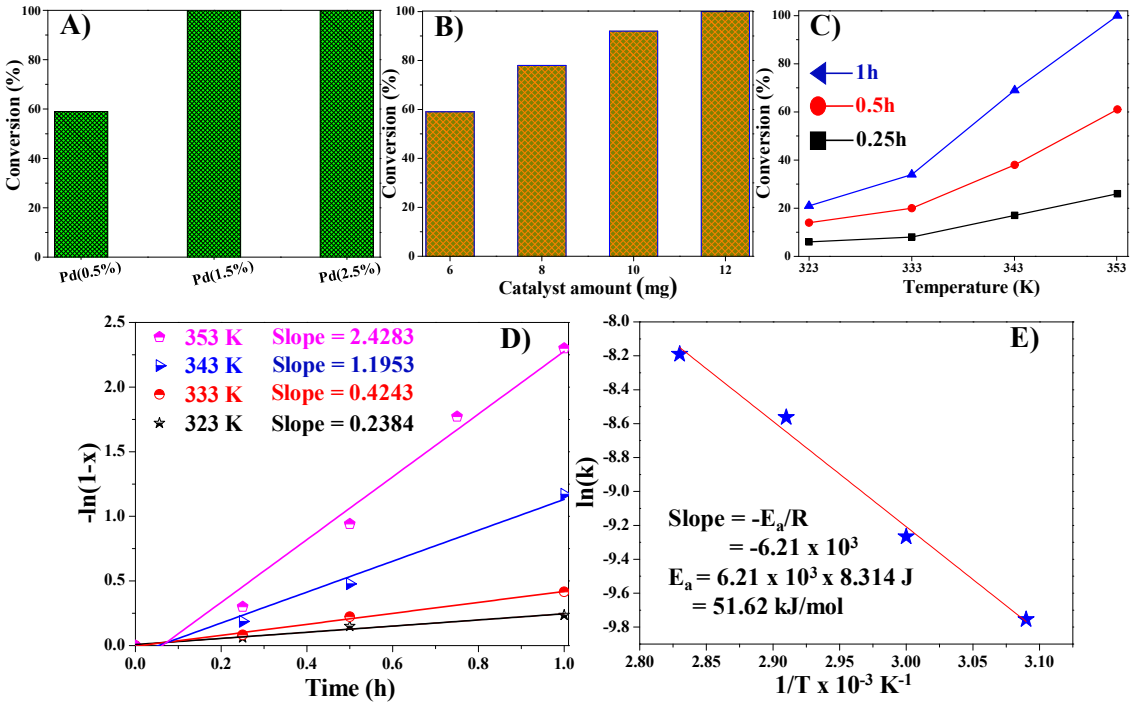

Fig. 5 Influence of (A) Pd loading, (B) catalyst amount, and (C) temperature-time for the C-O hydrogenolysis of BPE using Pd(1.5%)/Ce-BTC. (D) A plot of –ln(1-x) vs. time represents the kinetics study of the BPE hydrogenolysis, (E) and a plot of ln (k) vs 1/T (Arrhenius plot) for the BPE hydrogenolysis reaction.

Finally, an interesting result is obtained by studying the influence of solvent in the hydrogenolysis of BPE (Fig. S5). All the reactions are compared at 353 K after one hour of the reaction (except water). The reaction conducted in methanol affords the best activity at 353 K among the solvents investigated here. The reaction proceeds equally well in water when the reaction is performed at 383 K for two hours. To the best of our knowledge, this is one of the unique results when the BPE hydrogenolysis is reported in aqueous medium at such a low temperature of 383 K and an H_2 pressure of 2 bar. Although, the activity of catalysts in the water medium is two times lower than that of methanol, yet it is higher than that of several reported catalysts (Table 1). Moreover, similar activity to that of methanol is obtained at 353 K after one hour in the water when phase transfer catalyst (Tetrabutylammonium bromide) is employed. This result suggests that low activity of the catalyst in water is due to the limited solubility of BPE in the reaction medium. Thus, one can indicate that the catalyst is equally effective in the water medium provided that the reactant reaches the active sites.

View Article Online
DOI: 10.1039/D0CY01279C

Table 1 The comparative catalytic activity of Pd/Ce-BTC with various reported catalysts for the C-O hydrogenolysis of BPE.

S.N	Catalyst	Reaction condition	TOF (h^{-1})	Ref.
1	10%Ni-1%Ru/AC	BPE (1.08 mmol), MeOH (20 mL), catalyst (100 mg), H_2 (0.5 MPa), time (2 h), temp (393 K).	62.7	53
2	Fe-L1/C-800	BPE (1 mmol), water:THF (1:1) (20 mL), catalyst (100 mg), H_2 (2 Mpa), time (12 h), temp (513 K).	2.1	54
3	$Ti^{III}_2Ti^{IV}_6$-NiH (1 mol %)	BPE, heptanes, catalyst (100 mg), H_2 (1 bar), time (6 h), temp (413 K).	16.7	36
4	ReO_x/AC	BPE (100 mg), n-Hexane (15 mL), catalyst (30 mg), H_2 (3 Mpa), time (5 h), temp (473 K).	11.4	55
5	$Ru_{15}Ni_{85}$ NC	BPE (0.189 mmol), H_2O (1 mL), catalyst (0.00945 mmol), H_2 (1 atm), time (16 h), temp (368 K).	1.2	56
6	Ni/MoS_2 Ni-1.5%, Mo-5.1%	BPE: catalyst (10:1 mass ratio), dodecane H_2 (50 bar), time (0.5 h), temp (573 K).	138.5	57
7	Ni/AC	BPE (500 mg), MeOH (10 mL), catalyst (100 mg), H_2 (2 Mpa), time (2 h), temp (413 K).	8.0	58
8	TiN-Ni	BPE 0.05 M in EtOH, catalyst (0.8 g, 4.6 mmol of Ni), H_2 (12 bar), time (0.33 h), temp (398 K).	0.2	34
9	1%Ru-30%W/AC	BPE (100 mg), hexane (30 mL), catalyst (20 mg), H_2 (0.7 Mpa), time (10 h), temp (533 K).	1.6	59
10	$In(Otf)_3$+Ru/Al_2O_3	BPE (1 mmol), H_2O (1 mL), catalyst ($In(Otf)_3$ 0.05 mmol + 5 wt% Ru/Al_2O_3), H_2 (40 bar), time (2 h), temp (523 K).	6.8	60
11	Pd–Fe/OMC	BPE (500 mg), hexadecane (9 mL),	38.1	61

View Article Online
DOI: 10.1039/D0CY01279C

		catalyst (50 mg), H_2 (10 bar), time (1 h), temp (523 K).		
12	RuRe/MWCNT	BPE (0.24 g), n-heptane (24 mL), catalyst (50 mg), H_2 (20 bar), time (1 h), temp (473 K).	43.3	62
13	Ni/CB	BPE (0.0368 g), solvent (10 mL), catalyst (50 mg), H_2 (0.2 MPa), time (1 h), temp (473 K).	181.1	35
14	Pd(0.5%)/Ce-BTC	BPE (0.5 mmol), methanol (10 mL), catalyst (12 mg), H_2 (2 bar) time (1 h), temp (353 K).	526.8	This study
15	Pd(1.5%)/Ce-BTC	BPE (0.5 mmol), methanol (10 mL), catalyst (12 mg), H_2 (2 bar) time (1 h), temp (353 K).	312.5	This study

The hydrogenolysis of various lignin model compounds such as benzyl phenyl ether, 2-phenylethyl phenyl ether, and diphenyl ether are also investigated. The C-O bond dissociation energy for these compounds follows the order: benzyl phenyl ether (218 kJ mol^{-1}) < diphenyl ether (314 kJ mol^{-1}). At 353 K, BPE is completely converted, whereas no reaction occurs when 2-phenylethyl phenyl ether and diphenyl ether are reacted. Almost complete 2-phenylethyl phenyl ether conversion is obtained at 433 K in 8 h, whereas diphenyl ether requires 473 K and 12 h, for the complete conversion.

The catalyst stability and recyclability were evaluated for Pd(1.5%)/Ce-BTC in the BPE hydrogenolysis. After one hour of the reaction, the catalyst was separated by centrifugation, washed with ethanol, dried in a vacuum oven, and then used in the next cycle. Fig. S6A shows that the catalyst exhibits no appreciable change in the activity even after five catalytic cycles during the BPE hydrogenolysis. Moreover, a hot filtration test was also conducted for the BPE hydrogenolysis. After 0.25 h of the reaction, the catalyst was removed, and then the reaction was continued for the remaining 0.75 h to evaluate the progress of the reaction (Fig. S6B). GC analysis suggested that no reaction occurred after the removal of the catalyst, confirming that the reaction was heterogeneous, and no active species were leached in the solution, which could catalyze the reaction after the removal of the catalyst. MP-AES analysis confirmed that no leaching of Pd species was observed during the

View Article Online
DOI: 10.1039/D0CY01279C

reaction. The recycled catalyst was also characterized by XRD, volumetric analysis, SEM, TEM, and XPS investigations. No appreciable changes in the XRD pattern (Fig. S7A), surface area (S_{BET} = 45.3 m^2/g), and SEM image (Fig. S7B) of the catalyst are observed. The high-resolution TEM image of the spent catalyst suggests that the Pd is uniformly distributed in almost similar size to that of the fresh catalyst (Fig. S7C). Pd^0/Pd^{2+} ratio for the spent catalyst determined using a high-resolution Pd 3d XPS spectrum (Fig. S7D) is calculated to be 2.6 compared to 2.8 for the fresh catalyst. Recycling experiments and physiochemical characterizations of the spent catalyst indicate that the catalyst was stable during the reaction, and it can be used for multiple cycles.

To obtain the mechanistic insights and the reasons behind Pd/Ce-BTC's superior activity than Pd/CeO_2, the density functional theoretical (DFT) calculations were carried out. All the calculations were performed using generalized gradient approximation (GGA) with Perdew-Burke-Ernzerhof (PBE) exchange-correlation functional in conjunction with double numeric with depolarization (DND) basis set as implemented in DMol3 package.[60, 61] DFT study reveals the interactions between the reactant and the catalysts. The adsorption energies are computed by using the following equation,

$$E_{ads} = E_{(adsorbate+surface)} - E_{(adsorbate)} - E_{(surface)} \quad (1)$$

Where, $E_{(adsorbate+surface)}$ is the total energy of the catalyst surface adsorbed by BPE, $E_{(adsorbate)}$ is the energy of the BPE, and $E_{(surface)}$ is the energy of the catalyst surface. According to equation (1), the negative value of E_{ads} indicates the energetic feasibility of the adsorption on the catalyst surface. The asymmetric unit of MOF and a slice of the CeO_2 sheet are considered as a model system for the present study. In the case of CeO_2, the outer Ce and O atoms are frozen to reduce the computational time and to consider the central atoms as the reactive species. The optimized geometries of BPE, asymmetric unit of MOF, and CeO_2 sheet are shown in Fig. 6.

View Article Online
DOI: 10.1039/D0CY01279C

Fig. 6 The optimized geometries of BPE, asymmetric unit of MOF, and CeO_2 model systems obtained at the GGA-PBE/DND level of theory.

Initially, Pd is adsorbed to the different sites on the Ce-BTC and CeO_2 surfaces. The adsorption of Pd with the various sites of Ce-BTC is considered to obtain the most favorable binding site of Pd over the supporting materials *i.e.* Ce-BTC and CeO_2. Three different possible structures are optimized for the Pd adsorbed on Ce-BTC (Fig. S8). It is observed that during the interaction of the Pd NPs with the CeO_2 support, Pd is found to be occupied mostly around the oxygen surrounding sites. Furthermore, the partial charge distribution on the Pd sites obtained from the Hirshfeld charge analysis suggests that after Pd binding with the Ce-BTC and CeO_2 surface, Pd shows two different partial charge values. When Pd interacts with the Ce-BTC surface, the Hirshfeld charge of +0.19 eu is obtained. However, the Hirshfeld charge is increased to +0.69 eu when Pd binds with the CeO_2 surface. This shows that the Pd becomes positively charged after binding with the CeO_2 surface and this is the reason that more number of Pd is found in the +2 oxidation state in Pd/CeO_2 than that of the Pd/Ce-BTC. Hence, it is obvious to find a large fraction of Pd in +2 oxidation state in Pd/CeO_2 when compared to Pd/Ce-BTC. This observation further supports the Pd^0/Pd^{2+} ratio results obtained from the XPS analysis. It is well known that the Pd^0 dissociative adsorbs H_2 and forms the Pd-H active species, which exhibits C-O hydrogenolysis. Hence, the larger fraction of Pd^0 present in Pd/Ce-BTC MOF than that of Pd/CeO_2 is one of the possible reasons for the higher activity of Pd/Ce-BTC MOF than Pd/CeO_2. Further, the BPE is adsorbed over the stable catalyst surfaces (Pd/Ce-BTC and Pd/CeO_2) to compute the adsorption energies. The optimized geometries of catalyst surfaces adsorbed by BPE are shown in Fig. 7. For the complexes (A) and (B), the adsorption energies (E_{ads}) are found to be -2.29 eV and -1.65 eV, respectively. The higher adsorption energy in the case of Pd/Ce-BTC indicates that the adsorbate forms a stable complex. Furthermore, the larger bond length for C-O bond (5.17 a.u.) is also observed in this case, which suggests the weakening of the C-O

View Article Online
DOI: 10.1039/D0CY01279C

bond and the faster conversion of BPE into the products on the catalyst surface which supports the experimental observations.

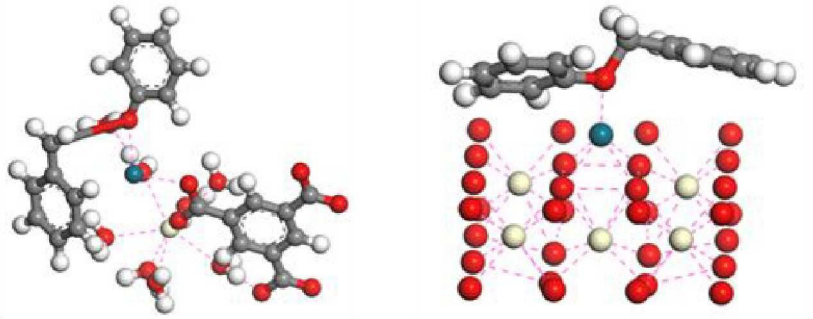

(A) (B)

Fig. 7 The optimized geometries of the adsorption of benzyl phenyl ether on the (A) Pd/Ce-BTC, and (B) Pd/CeO_2 catalyst surfaces obtained at the GGA-PBE/DND level of theory.

Moreover, the adsorption of the phenol (one of the hydrogenolysis product) on the catalyst surfaces is also computed. For the adsorption of phenol over Pd/Ce-BTC MOF and Pd/CeO_2 surfaces, the E_{ads} is obtained to be -0.89 eV and -1.34 eV, respectively. This indicates that the product forms an energetically more stable complex with the Pd/CeO_2, which makes desorption of the product difficult in this case as compared to the Pd/Ce-BTC MOF. This might be responsible for the lower yield of the products in the case of Pd/CeO_2 catalyst.

Catalytic and DFT results suggest that BPE adsorbs on the Ce-BTC and H_2 dissociative adsorbs on the Pd sites, simultaneously, *via* Langmuir-Hinshelwood mechanism. Then hydrogen atoms are transferred to the adsorbed BPE and produces toluene and phenol. Toluene diffuses out, and the phenol is bonded to the BPE adsorption sites. Finally, phenol desorbs and the catalytic sites are regenerated. XPS and DFT results suggest that more amount of Pd^0 is present in Pd/Ce-BTC; therefore, more numbers of Pd-H sites would be available for the hydrogenolysis. The higher adsorption energy for BPE on Ce-BTC and lower desorption energy for phenol on Pd/Ce-BTC are responsible for Pd/Ce-BTC's higher activity than Pd/CeO_2.

Conclusions

In summary, a highly dispersed, nanometer-sized, Pd nanoparticles decorated Ce-BTC MOF was successfully prepared. XPS analysis suggested that a higher concentration of Pd^0 species was present in Ce-BTC than in CeO_2, which were consistent with the DFT

View Article Online
DOI: 10.1039/D0CY01279C

calculations. DFT calculations showed that the Hirshfeld charge was more in Pd/CeO_2 than Pd/Ce-BTC which suggested that the Pd became positively charged after binding with the CeO_2 surface and higher concentration of Pd^{2+} were found in Pd/CeO_2 than Pd/Ce-BTC, thus; more numbers of Pd-H species would form in Pd(1.5%)/Ce-BTC upon H_2 adsorption. Pd(1.5%)/Ce-BTC exhibited excellent activity and selectivity in the hydrogenolysis of BPE under very mild reaction conditions of 353 K and 2 bar H_2 pressure. Additionally, low activation barrier for hydrogenolysis was observed over this catalyst compared to several reported catalysts. XPS and DFT calculations suggested that the higher concentration of Pd^0 species in Pd/Ce-BTC than Pd/CeO_2, the higher adsorption energy of BPE over Ce-BTC than Pd/CeO_2, lower desorption energy of phenol over Ce-BTC than CeO_2 were responsible for the higher activity of Pd/Ce-BTC. The detailed mechanistic evaluation, the mild reaction conditions, hydrogenolysis in methanol/water as a reaction medium, high TOF, efficient recyclability, and higher stability of the Pd/Ce-BTC catalyst under the employed conditions are several attractive features of this study which will attract significant attention of the researchers and industrialist.

Acknowledgements

The work is supported by DST-SERB, New Delhi (EMR/2016/001408). AK is grateful to MHRD through IIT Ropar for SRF fellowship. RS acknowledges the Faculty Research Innovation Award grant from IIT Ropar.

Author's contributions

RS and AKK planned work. AKK executed experimental work while SPK conducted computational work with the consultation of TJDK. RS and AKK wrote the manuscript.

Conflicts of interest

There are no conflicts to declare.

Electronic Supporting Information

Experimental procedures, detailed synthesis and characterization of catalysts, procedure of the catalytic reaction, TGA profiles, FE-SEM images, EF-TEM & EDS spectrum, XPS spectra, and recycling data are provided in this section.

View Article Online
DOI: 10.1039/D0CY01279C

References

1 P. Gallezot, *Chem. Soc. Rev.,* 2012, **41**, 1538−1558.

2 B. Liu and Z. Zhang, *ACS Catal.,* 2016, **6**, 326–338.

3 J. N. Putro, F. E. Soetaredjo, S.-Y. Lin, Y.-H. Ju and S. Ismadji, *RSC Adv.*, 2016, **6,** 46834–46852.

4 V. K. Ponnusamy, D. D. Nguyen, J. Dharmaraja, S. Shobana, J. R. Banu, R. G. Saratale, S. W. Chang and G. A Kumar, *Bioresour. Technol.,* 2019, **271**, 462–472

5 B. M. Matsagar, S. A. Hossain, T. Islam, H. R. Alamri, Z. A. Alothman, Y. Yamauchi, P. L. Dhepe, K. C. W. Wu, *Sci. Rep.,* 2017, **7**, 13946 (1-7).

6 B. R. Caes, R. E. Teixeira, K. G. Knapp and R. T. Raines, *ACS Sustainable Chem. Eng.,* 2015, **3**, 2591–2605.

7 P. Zhou and Z. Zhang, *Catal. Sci. Technol.,* 2016, **6**, 3694–3712.

8 A. Kumar and R. Srivastava, *Sustain. Energy Fuels*, 2019, **3**, 2475–2489.

9 K. Gupta, R. K. Rai and S. K. Singh, *ChemCatChem,* 2018, **10**, 2326–2349.

10 C. Xu, E. Paone, D. Rodríguez-Padrón, R. Luque and F. Mauriello, *Chem. Soc. Rev.*, 2020, **49**, 4273–4306.

11 A. J. Kumalaputri, G. Bottari, P. M. Erne, H. J. Heeres and K. Barta, *ChemSusChem,* 2014, *7*, 2266-2275.

12 G.-H. Wang, J. Hilgert and F. H. Richter, *Nat. Mater*., 2014, **13**, 293-300

13 C. H. Zhou, X. Xia, C. X. Lin, D. S. Tong and J. Beltramini, *Chem. Soc. Rev.*, 2011, **40**, 5588–5617.

14 A. J. Ragauskas, G. T. Beckham, M. J. Biddy, R. Chandra, F. Chen, M. F. Davis, B. H. Davison, R. A. Dixon, P. Gilna and M. Keller, *Science,* 2014, **344**, 1246843(1-10)

15 R. Rinaldi, R. Jastrzebski, M. T. Clough, J. Ralph, M. Kennema, P. C. Bruijnincx and B. M. Weckhuysen, *Angew Chem. Int. Ed.,* 2016, **55**, 8164-8215

16 P. A. Lazaridis, A. P. Fotopoulus, S. A. Karakoulia and K. S. Triantafyllidis, *Front. Chem*., 2018, **6**, 295 (1-21).

17 C. Yong, W. Wen-Liang and C. Jian-Min, *J. Biobased Mater.,* 2020, **14**, 120–125.

18 C. Liu, S. Wu, H. Zhang and R. Xiao, *Fuel Process. Technol.,* 2019, **191**, 181–201.

19 V. E. Tarabanko and N. Tarabanko, *Int. J. Mol. Sci.,* 2017, **18**, 2421 (1–29).

20 J-M. Ha, K-R. Hwang, Y-M. Kim, J. J. Kwang, H. Kim, H. W. Lee, J-Y. Kim, Y-K. Park, *Renew. Sust. Ener.* Rev., 2019**, 111**, 422-441

21 M. Zaheer and R. Kempe, *ACS Catal.,* 2015, **5**, 1675−1684.

View Article Online
DOI: 10.1039/D0CY01279C

22 S. C. Qi, J. I. Hayashi, S. Kudo and L. Zhang, *Green Chem.,* 2017, **19**, 2636–2645.

23 L. P. Xiao, S. Wang, H. Li, Z. Li, Z. J. Shi, L. Xiao, R. C. Sun, Y. Fang and G. Song, *ACS Catal.* 2017, **7**, 7535–7542.

24 T. Renders, G. V. Bossche, T. Vangeel, K. V. Aelst and B. Sels, *Curr. Opin. Biotechnol.* 2019, **56**, 193-201.

25 E. Paone, T. Tabanelli and F. Mauriello, *Curr. Opin. Green. Sustain. Chem*. 2020, **24**, 1-6.

26 A. G. Sergeev, J. D. Webb and J. F. Hartwing, *J. Am. Chem. Soc.,* 2012, **134**, 20226−20229.

27 S. Son and F. D. Toste, *Angew. Chem. Int. Ed.,* 2010, **49**, 3791 –3794.

28 J. M. Nichols, L. M. Bishop, R. G. Bergman and J. A. Ellman, *J. Am. Chem. Soc.,* 2010, **132**, 12554 –12555

29 B. S. Samant and G. W. Kabalka, *Chem. Commun.,* 2012, **48**, 8658 –8660;

30 M. Tobisu, K. Yamakawa, T. Shimasaki and N. Chatani, *Chem. Commun.,* 2011, **47**, 2946 –2948.

31 X. Wang and R. Rinaldo, *ChemSusChem,* 2012, **5**, 1455 –1466.

32 T. H. Parsell, B. C. Owen, I. T. Klein, M. Jarrell, C. L. Marcum, L. J. Haupert, L. M. Amundson, H. I. Kenttmaa, F. J. Ribeiro, T. Miller and M. M. Abu-Omar, *Chem. Sci.,* 2013, **4**, 806–813.

33 J. He, C. Zhao and J. A. Lercher, *J. Am. Chem. Soc.,* 2012, **134**, 20768–20775.

34 M. Zaheer, J. Hermannsdçrfer, W. P. Kretschmer, G. Motz and R. Kempe, *ChemCatChem* 2014, **6**, 91–95.

35 B. M. Matsagar, T-C. Kang, Z-Y. Wang, T. Yoshikawa, Y. Nakasaka, T. Masuda, L-C. Chuangc, C.-W. K. Wu, *React. Chem. Eng.*, 2019, **4**, 618–626.

36 Y. Song, Z. Li, P. J, Kaufmann, M. X. Feng, J. S. Chen, C. Wang and W. Lin, *ACS Catal.,* 2019, **9**, 1578−1583.

37 V. Molinari, C. Giordano, M. Antonietti and D.Esposito, *J. Am. Chem. Soc.,* 2014, **136**, 1758−1761.

38 A. P. V. Muyden, S. Siankevich, N. Yan and P. J. Dyson, *ChemCatChem,* 2019, **11**, 2743–2752.

39 E. Paone, C. Espro, R. Pietropaoloa and F. Mauriello, *Catal. Sci. Technol.,* 2016, **6**, 7937–7941.

40 D. Forberg, T. Schwob, M. Zaheer, M. Friedrich, N. Miyajima and R. Kempe,

View Article Online
DOI: 10.1039/D0CY01279C

Nature Commun., 2016, **7**, 13201 (1-6).

41 D. Divakar, D. Manikandan, V. Rupa, E. L. Preethi, R. Chandrasekar and T.Sivakumar, *J Chem Technol Biotechnol.,* 2007, **82**, 253–258.

42 M. C. Quesada, A. Yarulin, M. Jin, Y. Xia, L. K. Minsker, *J. Am. Chem. Soc.,* 2011, **133**, 12787–12794.

43 D. N. Semagina, A. Renken and L. K. Minsker, *J. Phys. Chem. C.,* 2007, **111**, 13933–13937.

44 A. Tsuda and N. V. Konduru, *NanoImpact,* 2016, **2**, 38–44.

45 K. K. Nanda, A. Maisels, F. E. Kruis, H. Fissan and S. Stappert, *Phy. Rev. Lett.* 2003, **91**, 1061021-24.

46 A. Cao, R. Lu and G. Veser, *Phys. Chem. Chem. Phy.,* 2010, **12**, 13499–13510.

47 W. Zhang, G. Lu, C. Cui, Y. Liu, S. Li, W. Yan, C. Xing, Y. R. Chi, Y. Yang and F. Huo, *Adv. Mater.,* 2014, **26**, 4056–4060.

48 A. Corma, H. Garcia and F. X. L. Xamena, *Chem. Rev.,* 2010, **110**, 4606–4655.

49 A. H. Chughtai, N. Ahmad, H. A. Younus, A. Laypkov and F. Verpoort, *Chem. Soc. Rev.,* 2015, **44**, 6804-6849.

50 A. Dhakshinamoorthy and H. Garcia, *Chem. Soc. Rev.,* 2012, **41**, 5262–5284.

51 Y. H. Wen, J. K. Cheng, Y. L. Feng, J. Zhang, Z. J. Li and Y. G. Yao, *Chin. J. Struct. Chem.,* 2005, **24**, 1440-1444.

52 K. Liu, H. You, G. Jia, Y. Zheng, Y. Huang, Y. Song, M. Yang, L. Zhang and H. Zhang, *Cryst. Growth Des.,* 2010, **10**, 790-797.

53 C. Zhu, J. P. Cao, X. Y. Zhao, T. Xie, M. Zhao and X. Y. Wei, *Fuel Process. Technol.,* 2019, **194**, 106126.

54 J. Li, H. Sun, J. X. Liu, J. J. Zhang, Z. X. Li and Y. Fu, *Mol. Catal.,* 2018, **452**, 36–45.

55 B. Zhang, Z. Qi, X. Li, J. Ji, W. Luo, C. Li, A. Wang and T. Zhang, *ACS Sustainable Chem. Eng.,* 2019**,** ***7***, 208−215.

56 S. Bulut, S. Siankevich, A. P. Muyden, D. T. L. Alexander, G. Savoglidis, J. Zhang, V. Hatzimanikatis, N. Yan and P. J. Dyson, *Chem. Sci.,* 2018, **9**, 5530–5535.

57 S. Mukundan, L. Atanda and J. Beltramini, *Sustain. Energy Fuels*, 2019, **3**, 1317-1328.

58 C. Zhu, J. P. Cao, X. Y.; Zhao, T. Xie, J. Ren and X. Y. Wei, *J. Energy Inst.,* 2019, **92**, 74-81.

View Article Online
DOI: 10.1039/D0CY01279C

59 J. Ji, H. Guo, C. Li, Z. Qi, B. Zhang, T. Dai, M. Jiang, C. Ren, A. Wang and T. Zhang. *ChemCatChem*, 2018, **10**, 415–421.

60 H. Wang, Y. Duan, Q.. Zhang and B. Yang, *ChemSusChem,* 2018, **11**, 2562 – 2568.

61 J. K. Kim, J. K. Lee, K. H. Kang, J. C. Song and I. K. Song, *Appl. Catal. A-Gen.* 2015, **498**, 142–149.

62 K. B. Jung, J. Lee, J. M. Ha, H. Lee, D. J. Suh, C. H. Jun and J. Jae, *Catal. Today,* 2018, **303**, 191–199.

63 B. Delley, *J. Chem. Phys.,* 1990, **92**, 508−517.

64 B. Delley, *J. Chem. Phys.,* 2000, **113**, 7756−7764.

View Article Online
DOI: 10.1039/D0CY01279C

Table of Contents

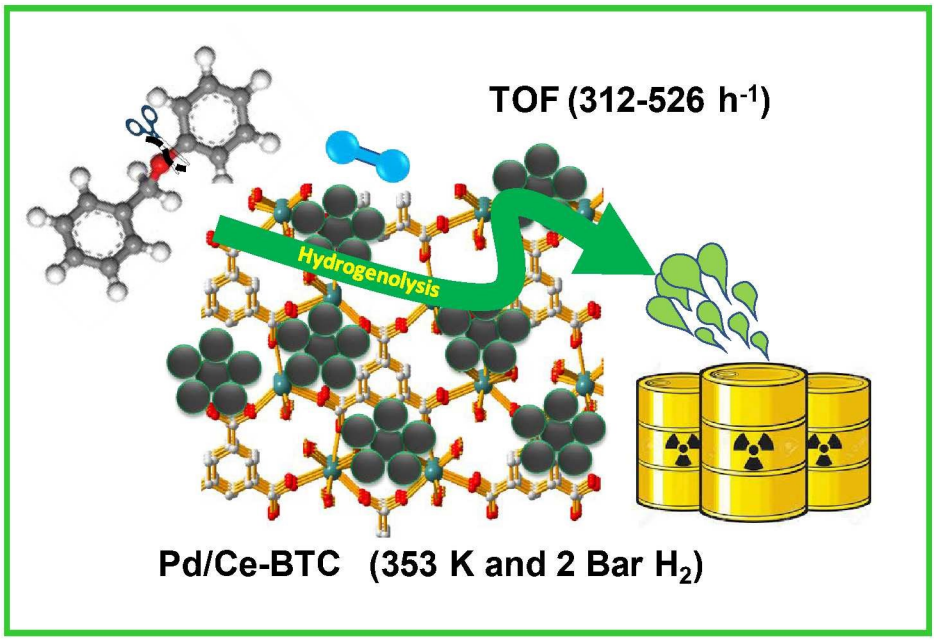

Significant Pd^0 content (higher Pd^0/Pd^{2+} ratio) and optimum bonding of reactant & product (higher adsorption energy of benzyl phenyl ether and lower desorption energy for product phenol) are responsible for the exceptional catalytic activity of Pd/Ce-MOF at mild reaction conditions.